Optimum Bias Conditions for Linear Broad-Band InGaP/GaAs HBT Power Amplifiers

Masaya Iwamoto, *Student Member, IEEE*, Craig P. Hutchinson, Jonathan B. Scott, *Senior Member, IEEE*, Thomas S. Low, Mani Vaidyanathan, *Member, IEEE*, Peter M. Asbeck, *Fellow, IEEE*, and Donald C. D'Avanzo, *Member, IEEE*

***Abstract*—A design strategy for a linear broad-band InGaP/GaAs heterojunction bipolar transistor (HBT) power amplifier is presented. This design is based on the bias dependence of the nonlinear base–collector charge, as expressed in the $C_{\rm BC}$ versus $V_{\rm CE}$ and τ_C versus I_C characteristics of the device. Using this technique, it is shown that the second- and third-order distortions have separate optimum bias conditions and, furthermore, there is an inherent tradeoff in optimizing the second- and third-order distortions. The strong bias dependence of the nonlinear base–collector charge and the tradeoff between the different orders of distortion are verified on two 24-dBm 0.5–11-GHz distributed power amplifiers optimized for second- and third-order distortions, respectively. The experimental results show that the harmonic and intermodulation levels are sensitive to the different order derivatives of the f_t versus I_C curve. Specifically, second-order distortion is related to the slope of the f_t versus I_C curve and third-order distortion is related to both the slope and curvature of the f_t versus I_C curve. This design technique suggests the importance of HBT device design to minimize distortion in high-frequency broad-band amplifier designs. Furthermore, to minimize high-frequency distortion in HBT amplifiers across a wide range of bias, it is desirable to linearize the base–collector charge, where flat $C_{\rm BC}$ versus $V_{\rm CE}$ and f_t versus I_C characteristics are ideally desired.**

***Index Terms*—Distortion, heterojunction bipolar transistor (HBT), RF power amplifier.**

I. Introduction

LINEAR broad-band power amplifiers with bandwidths greater than a decade have numerous commercial applications. In the area of test instrumentation, wide bandwidth sources with low harmonic distortion are essential since power is swept over a wide range of frequencies, which makes filtering impractical. Linear wide-bandwidth amplifiers are also important in cable television distribution, where low harmonic-distortion gain stages are desired for similar reasons. Typically in these applications, high bandwidth and linearity are critical specifications, and efficiency is a less important requirement. One of the major challenges in designing broad-band power amplifiers is to maintain high linearity over the entire bandwidth since narrow-band linearization techniques cannot be utilized. In this paper, we present an intuitive design methodology for an InGaP/GaAs heterojunction bipolar transistor (HBT) broad-band power amplifier, which achieves high linearity over a wide range of frequencies based on properly identifying linear bias points from s-parameter data. More specifically, the optimum bias points are chosen by observing the nonlinear behavior of the base–collector capacitance $(C_{\rm BC})$ with collector–emitter voltage and the unity current gain frequency (f_t) with collector current.

Background on the sources and mechanisms of distortion in HBTs, focusing on base–collector charge, is discussed in Section II. Experimental results of the influence of $C_{\rm BC}$ and f_t on harmonic distortion are described in detail. In Section III, simple expressions based on a simplified small-signal model are derived to show the link between f_t and linearity figures-of-merit second–order intercept point (IP2) and third-order intercept point (IP3). Using the intuitions gained in these sections, a design strategy for a linear broad-band amplifier based on the distributed amplifier is presented in Section IV. Two amplifiers optimized for second- and third-order distortions are described. Finally, in Section V, experimental results of the two amplifiers are presented to demonstrate the effectiveness of the low-distortion broad-band design technique.

II. Background on Nonlinearities in HBTs

Experimental studies of the distortion behavior of HBTs have identified several significant sources of nonlinearities of the device. Among these, the most prominent is the nonlinearity of the output current as a function of input voltage, quantified by the transconductance g_m. This g_m nonlinearity is very strong at the $V_{\rm BE}$ turn-on voltage (i.e., at low-current levels) and gradually becomes linearized by the extrinsic base and emitter resistances as current is increased [1]. At higher frequencies, nonlinearities due to capacitances (or charges, in general) become a significant source of distortion. It has been shown that the nonlinearity due to the $V_{\rm CE}$ dependence of $C_{\rm BC}$ is a significant contributor to distortion [2], [3]. Additionally, it has been shown experimentally that the nonlinearity due to the transit time is also a significant contributor to device distortion [4]. In Sections II-A–C, the bias dependence of intermodulation and harmonic distortions is explored, with emphasis on the role of the nonlinearity of the base–collector charge.

Manuscript received April 5, 2002; revised August 26, 2002. This work was supported in part by the Center for Wireless Communications, University of California at San Diego.

M. Iwamoto, M. Vaidyanathan, and P. M. Asbeck are with the Department of Electrical and Computer Engineering, University of California at San Diego, La Jolla, CA 92092 USA.

C. P. Hutchinson, J. B. Scott, T. S. Low, and D. C. D'Avanzo are with the Microwave Technology Center, Agilent Technologies, Santa Rosa, CA 95453 USA.

Digital Object Identifier 10.1109/TMTT.2002.805135

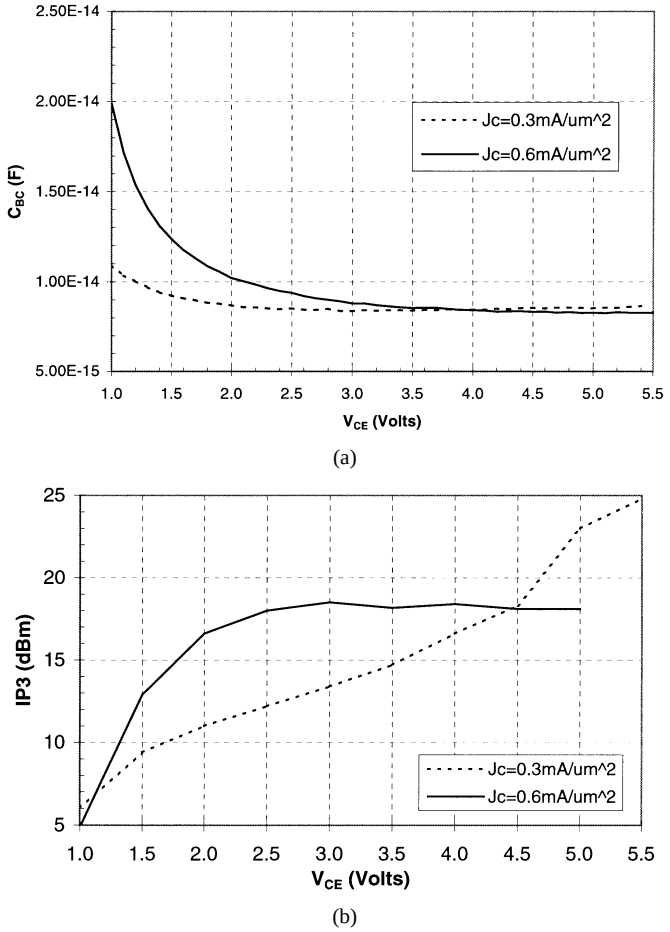

Fig. 1. (a) Measured $C_{\rm BC}$ versus $V_{\rm CE}$ at $J_C = 0.3$ and 0.6 mA/μm^2. (b) Measured IP3 versus $V_{\rm CE}$ at $J_C = 0.3$ and 0.6 mA/μm^2.

A. Intermodulation Distortion

The bias dependence of intermodulation distortion at high frequencies was experimentally investigated in detail in [4] so only a brief overview of those results will be presented here. Numerous papers have reported a link between the $C_{\rm BC}$ versus $V_{\rm CE}$ characteristics of the device and intermodulation distortion [2], [3]. Fig. 1(a) shows a measurement of $C_{\rm BC}$ versus $V_{\rm CE}$ measured at two different current densities, i.e., 0.3 and 0.6 mA/μm^2. The device is an InGaP/GaAs HBT with a collector thickness of 0.7 μm and doping of 0.85×10^{16} cm^{-3} (equivalent to the device "HBT-C" in [4]). Fig. 1(b) shows a measurement of IP3 versus $V_{\rm CE}$ at the same current densities for this device based on two-tone measurements. The measurement conditions correspond to a frequency of 5 GHz, a frequency spacing of 1 MHz, and a load impedance of 260 Ω. In general, IP3 improves as $V_{\rm CE}$ is increased since IP3 is a function of the derivatives of the $C_{\rm BC}$ versus $V_{\rm CE}$ curve. This trend is clear for the $J_C = 0.6$ mA/μm^2 case, where IP3 flattens out approximately when $C_{\rm BC}$ becomes a constant value. However, this trend is not always observed, for example, as in the case for $J_C = 0.3$ mA/μm^2. Here, IP3 has a lower value even though $C_{\rm BC}$ versus $V_{\rm CE}$ behavior is flatter than at $J_C = 0.6$ mA/μm^2 ($C_{\rm BC}$ in both cases are influenced by the Kirk effect). In this particular case, the transit time nonlinearities have a significant influence at this current density. Fig. 2 shows a plot of IP3 versus

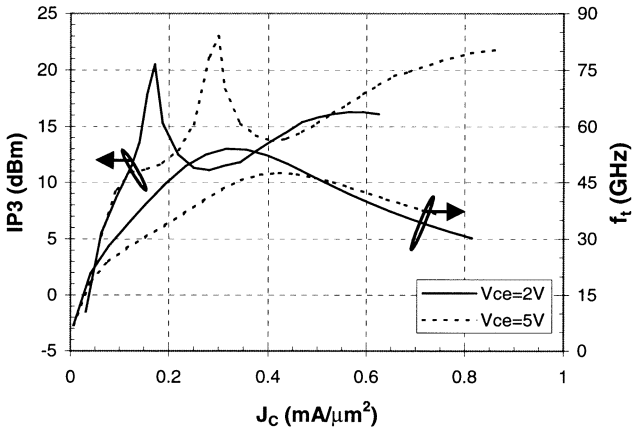

Fig. 2. Measured IP3 versus J_C and f_t versus J_C at $V_{\rm CE} = 2$ and 5 V.

J_C and f_t versus J_C at $V_{\rm CE}$ of 2 and 5 V. f_t is related to transit time since $1/2\pi f_t$ is equal to the total emitter–collector delay time. It can be qualitatively seen that there is a relationship between the curvature of f_t versus J_C and the value of IP3, where large curvature results in lower IP3. The strong peaks in IP3 are due to the transit time nonlinearity reaching a minimum at these bias points. These effects will be investigated in more detail analytically in Section III. At $V_{\rm CE} = 2$ V, the curvature of the f_t versus J_C curve is near its maximum at 0.3 mA/μm^2, which explains why IP3 is low at this bias point. As $V_{\rm CE}$ is increased, the current density position in the peak f_t is shifted toward a higher value (due to the voltage dependence of Kirk effect [5]), and IP3 is improved at this current density. Finally, at $V_{\rm CE} = 5$ V and $J_C = 0.3$ mA/μm^2, IP3 reaches its peak value on the IP3 versus J_C curve. Additionally, in Fig. 2, it is evident that IP3 values are similar for both $V_{\rm CE}$ cases at low currents. This is attributed to the fact that g_m nonlinearities dominate in this region. The results in Figs. 1 and 2 demonstrate that the $C_{\rm BC}$ versus $V_{\rm CE}$ and f_t versus J_C characteristics are important parameters to monitor in understanding the distortion characteristics of HBTs.

B. Harmonic Distortion

Harmonic distortion was investigated in a similar fashion. The measurements were taken on similar devices, and the f_t versus J_C and $V_{\rm CE}$ characteristics are shown in Fig. 3. In this three-dimensional plot, the current density for peak f_t increases with $V_{\rm CE}$, as expected from theory.

Fig. 4(a) shows a plot of second harmonic intercept point (IP2h) of the same device measured at 5 GHz and a load impedance of 50 Ω. The definition of IP2h is analogous to IP3, but is based on the second harmonic power and extrapolated from a single-tone measurement. There is a very striking relation between this plot and the f_t plot in Fig. 3, in which the bias points where the peaks of both IP2h and f_t occur match very closely. This trend has also been observed experimentally for Si bipolar junction transistors (BJTs) [6]. Qualitatively, the second harmonic distortion is related to the slope of the f_t versus J_C curve. A more analytical treatment of this phenomenon will be discussed in Section III.

In Fig. 4(b), a plot of the third harmonic intercept point (IP3h) is shown over the same range of bias. The definition of IP3h is

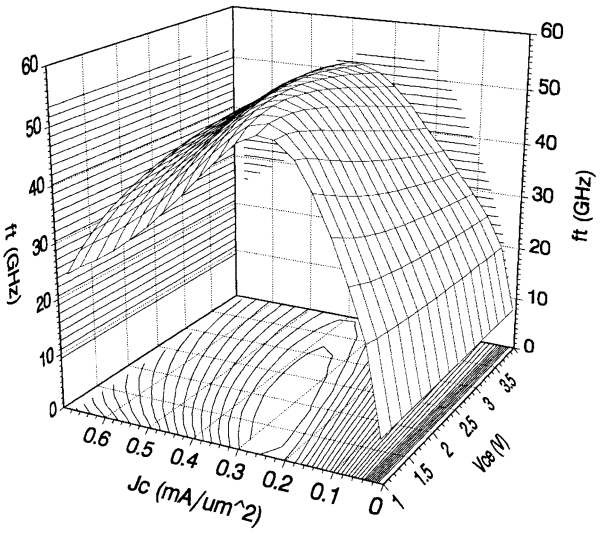

Fig. 3. Measured f_t versus J_C and $V_{\rm CE}$.

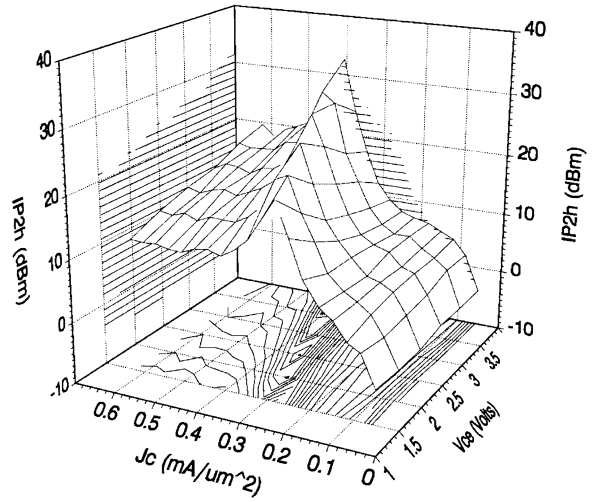

(a)

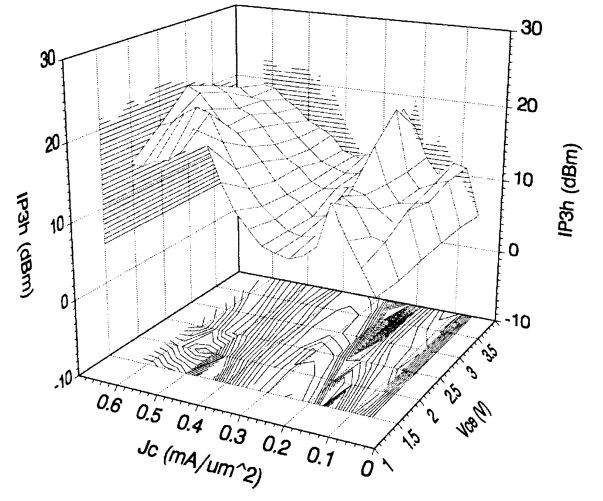

(b)

Fig. 4. (a) Measured IP2h versus J_C and $V_{\rm CE}$. (b) Measured IP3h versus J_C and $V_{\rm CE}$.

similar to IP2h, but based on third harmonic power measurements. An interesting feature of this plot is its resemblance to the IP3

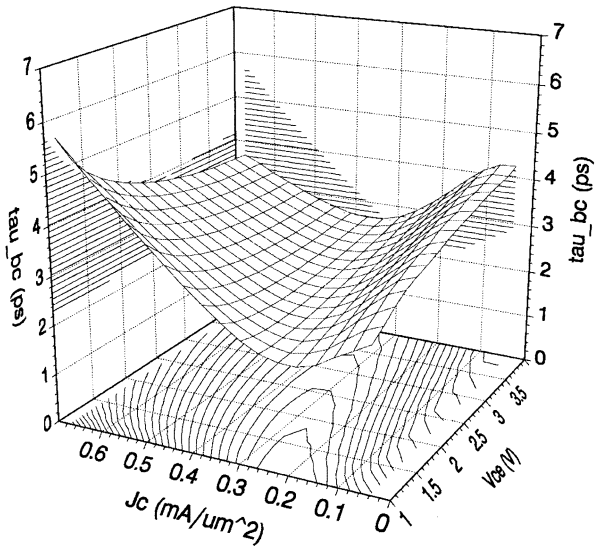

Fig. 5. Estimated base–collector transit time versus J_C and $V_{\rm CE}$ extracted from s-parameter data.

plot shown in Section II-A. It is clear that there is a sharp peak followed by a trough, which coincides with the region where the f_t peaks. Therefore, it is apparent that third-order intermodulation and harmonic distortions share similar mechanisms.

C. Base–Collector Transit Time

Since the bias dependence and derivatives of f_t are important factors determining distortion, it is meaningful to narrow down the sources of nonlinearity of f_t. f_t is related to the total emitter–collector delay ($\tau_{\rm EC}$) by the well-known expression

$$\tau_{\rm EC} = \frac{1}{2\pi f_t} = (R_E + R_C)C_{\rm BC} + \frac{kT}{qI_C}(C_{\rm BC} + C_{\rm BE}) + \tau_B + \tau_C. \quad (1)$$

The first term is typically small compared to the other terms and the second term becomes negligible at high current densities. By removing the first two terms (after extracting $C_{\rm BC}$, $C_{\rm BE}$, R_E, and R_C), we are left with the base–collector transit time ($\tau_{\rm BC}$), which consists of the base and collector transit times (τ_B and τ_C, respectively). A plot of this quantity (as estimated on the basis of S-parameter measurements) is shown in Fig. 5.

Fig. 5 shows that the nonlinear behavior of transit time at high currents is influenced by τ_B and τ_C. τ_B represents the delay associated with the minority carrier transport across the base region, including the current-induced base region due to Kirk effect. τ_C represents the delay associated with electrons traversing the collector depletion region. At high current densities below the onset of Kirk effect, the nonlinear behavior of f_t is predominantly influenced by τ_C due to the complex variation of electron velocity with the electric-field profile in the collector depletion region. As current density increases at a fixed base–collector voltage, the effective space charge density in the collector depletion region decreases, which causes a decrease in the effective electric field near the base edge of the collector [7]. Due to the negative differential mobility characteristics of

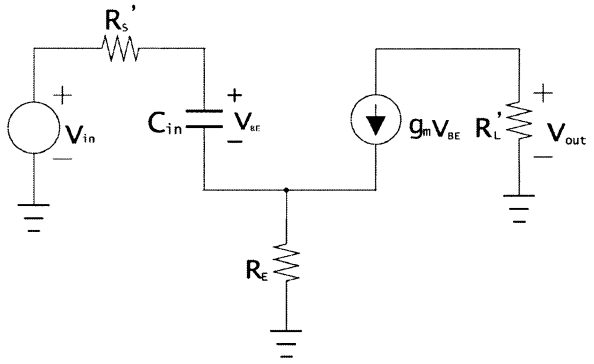

Fig. 6. Small-signal model used for nonlinear analysis.

GaAs, this decrease in field translates to an increase in electron velocity. Therefore, this phenomenon (sometimes referred to as "f_t peaking") causes a decrease in $\tau_{\rm BC}$ (or specifically τ_C) as the collector current is increased up until the onset of Kirk effect [8]. τ_B, on the other hand, does not become significantly nonlinear until base-pushout occurs past the Kirk effect threshold current. Since the significant peaks in the second- and third-order distortions (representing optimum bias points) occur in the vicinity of Kirk effect, it can be concluded that τ_C (in addition to τ_B) has an important influence on both intermodulation and harmonic distortion characteristics of HBTs.

It is important to note that $C_{\rm BC}$ and τ_C are related to each other since $C_{\rm BC}$ and τ_C are derivatives of the base–collector charge $(Q_{\rm BC})$ with respect to $V_{\rm BC}$ and I_C, respectively. Therefore, it can be said that the nonlinearities associated with $C_{\rm BC}$ and τ_C are tied to a single nonlinear source $Q_{\rm BC}$. It is also interesting that the nonlinear behavior of electron velocity with electric field of the GaAs collector (due to inter-valley transfer of electrons in the conduction band) directly influences the distortion characteristics of GaAs HBTs.

III. Analysis of Base–Collector Charge Nonlinearity

Simple relationships between f_t and linearity figures-of-merit IP2 and IP3 are derived here. The analysis is based on the simple small-signal model shown in Fig. 6. Circuit elements have been lumped together to simplify the analysis. R'_S represents the total source resistance (including base resistance contributions) and R'_L represents the total load resistance (including collector resistance). The charge of the device is assumed to be dominated by the input capacitance, $C_{\rm in}$. $C_{\rm in}$ includes the effect of $C_{\rm BC}$ (augmented by the Miller effect) and is given by

$$C_{\rm in} = \frac{g_m}{2\pi f_t^*} = \frac{g_m}{2\pi f_t} + g_m R'_L C_{\rm BC} \tag{2}$$

where f_t^* is the unity current gain frequency with a load resistance R'_L ("loaded f_t").

The relationship between the output and input voltages are derived to be

$$v_{\rm out} = \left(\frac{-R'_L}{\dfrac{1}{g_m} + R_E + j\dfrac{2\pi f C_{\rm in}}{g_m}\Big(R'_S + R_E\Big)} \right) v_{\rm in}. \tag{3}$$

By substituting (2), we get

$$v_{\rm out} = \left(\frac{-R'_L}{\dfrac{1}{g_m} + R_E + j\dfrac{f}{f_t^*}\Big(R'_S + R_E\Big)} \right) v_{\rm in}. \tag{4}$$

To simplify the expression further, a high-frequency approximation $(f/f_t^*) \gg (1/g_m + R_E)/(R'_S + R_E)$ is made, which results in

$$v_{\rm out} = \left(\frac{-R'_L f_t^*}{jf\Big(R'_S + R_E\Big)} \right) v_{\rm in}. \tag{5}$$

The nonlinearity of the circuit is contained in the fact that f_t^* is a function of I_C and $V_{\rm CE}$. As the output voltage $v_{\rm out}$ varies as $\Delta v_{\rm out} = v_{\rm out} \sin \omega t$, I_C and $V_{\rm CE}$ vary according to $\Delta V_{\rm CE} = -\Delta v_{\rm out}$ and $\Delta I_C = -\Delta v_{\rm out}/R'_L$. f_t^* is expanded as an approximation given by

$$f_t^* = f_{to}^* + \frac{\partial f_t^*}{\partial I_C}\Delta I_C + \frac{\partial f_t^*}{\partial V_{\rm CE}}\Delta V_{\rm CE} + \frac{1}{2}\frac{\partial^2 f_t^*}{\partial I_C^2}\Delta I_C^2 + \frac{1}{2}\frac{\partial^2 f_t^*}{\partial V_{\rm CE}^2}\Delta V_{\rm CE}^2 + \frac{\partial^2 f_t^*}{\partial I_C \partial V_{\rm CE}}\Delta I_C \Delta V_{\rm CE} + \cdots. \tag{6}$$

As shown in Fig. 3, the variation of f_t with I_C is significantly larger than with $V_{\rm CE}$, thus, the derivatives with respect to $V_{\rm CE}$ can be approximately neglected. Also, at larger values of $V_{\rm CE}$ ($V_{\rm CE} > 3$ V in the case of the device in Section II), the $V_{\rm CE}$ dependent nonlinearity due to $C_{\rm BC}$ becomes small, and this nonlinearity is neglected in the analysis.

Substituting (6) into (5), we obtain the incremental output voltage

$$\Delta v_{\rm out} = K\left(f_{to}^* - \left(\frac{1}{R'_L}\right)\left(\frac{\partial f_t^*}{\partial I_C}\right)\Delta v_{\rm out}\Delta v_{\rm in} + \left(\frac{1}{2R'^2_L}\right)\left(\frac{\partial^2 f_t^*}{\partial I_C^2}\right)\Delta v_{\rm out}^2 \Delta v_{\rm in} + \cdots \right) \tag{7}$$

where the derivatives are evaluated along the load line. This equation is of the form

$$\Delta v_{\rm out} = h_1 \Delta v_{\rm in} + h_2 \Delta v_{\rm in}\Delta v_{\rm out} + h_3 \Delta v_{\rm out}^2 \Delta v_{\rm in} + \cdots. \tag{8}$$

To obtain the desired output–input relationship

$$\Delta v_{\rm out} = k_1 \Delta v_{\rm in} + k_2 \Delta v_{\rm in}^2 + k_3 \Delta v_{\rm in}^3 + \cdots \tag{9}$$

the substitutions $k_1 = h_1$, $k_2 = h_2 h_1$, and $k_3 = h_2^2 h_1 + h_3 h_1^2$ are made.

Using the relationship between IPn and the k_n coefficients

$$\mathrm{IP}n = B_n \left[\frac{|k_1|^{2n}}{|k_n|^2} \right]^{(1/n-1)} \tag{10}$$

approximations for IP2 and IP3 are made as follows:

$$\frac{1}{\rm IP2} \sim \left(\frac{1}{f_t^*}\frac{\partial f_t^*}{\partial I_C} \right)^2 \tag{11}$$

$$\frac{1}{\rm IP3} \sim \left(\frac{1}{f_t^*}\frac{\partial f_t^*}{\partial I_C} \right)^2 + \frac{1}{2f_t^*}\frac{\partial^2 f_t^*}{\partial I_C^2}. \tag{12}$$

Fig. 7(a) shows an f_t versus J_C plot obtained from simulations of a large-signal HBT model [4], [12] at $V_{\rm CE} = 4$ V of a

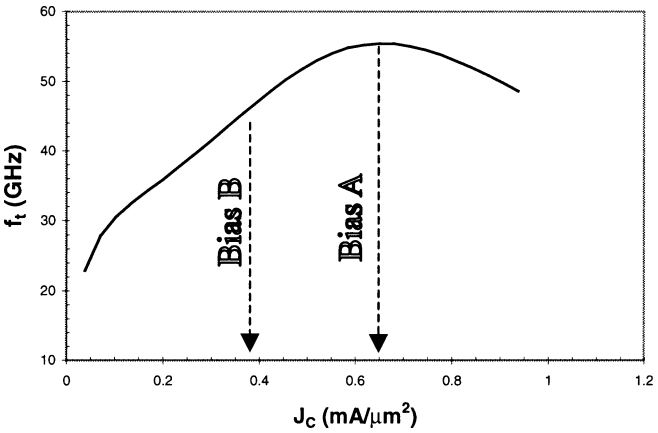

(a)

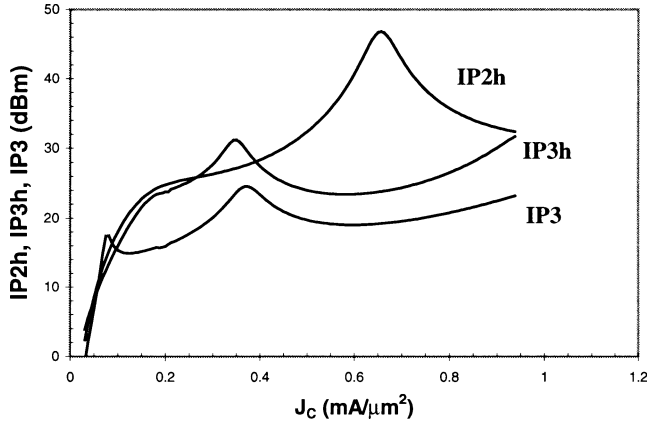

(b)

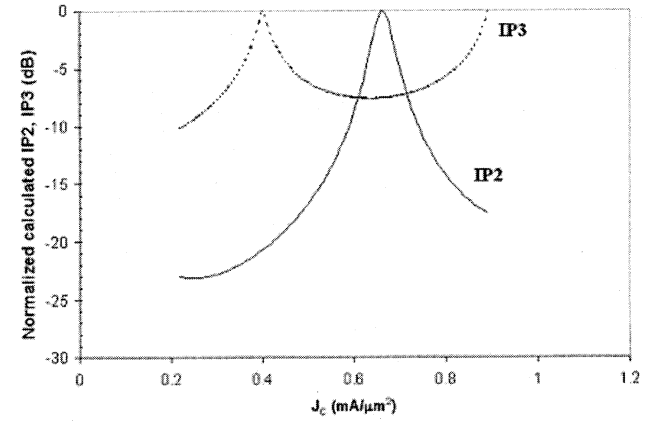

(c)

Fig. 7. (a) f_t versus J_C *simulated with a large-signal HBT model* [4], [12] at $V_{\rm CE} = 4$ V. (b) *Simulated* IP2h, IP3h, and IP3 versus J_C at $V_{\rm CE} = 4$ V. (c) Normalized calculated IP2 and IP3 versus J_C.

representative HBT device, and Fig. 7(b) shows corresponding distortion curves. At this $V_{\rm CE}$ bias, the collector is fully depleted and the nonlinear contribution from $C_{\rm BC}$ should be very low. Applying (11) and (12) using the f_t data in Fig. 7(a), an estimate of where the peaks and troughs occur in the distortion curves can be made, as shown in Fig. 7(c). Fig. 7(c) was simply constructed by performing a polynomial fit to the f_t versus J_C characteristics of Fig. 7(a), and then applying (11) and (12) with arbitrary constants (representing other sources of distortion) to adjust the levels of IP2 and IP3. The agreement between the shapes of the corresponding curves is striking.

Equation (11) states that to minimize second-order distortion due to transit time, the device should be biased at a current where the slope of f_t versus I_C is at a minimum and the magnitude of f_t is at a maximum. Fortunately, these two conditions are simultaneously met at the f_t peak, denoted by Bias A in Fig. 7(a). According to (12), the third-order distortion due to transit time is more complex since both the slope and curvature of f_t are involved. It can be seen from Fig. 7(b) and (c) that any significant curvature in the f_t versus J_C characteristics is detrimental to third-order distortion. Accordingly, a local minimum in IP3 exists where the curvature is at a maximum (at peak f_t) and the peak in IP3 occurs where the curvature is small at Bias B. More specifically, the peak in IP3 occurs when the sum of the terms in (12) is at a minimum. Since the slope and curvature cannot be typically minimized simultaneously (unless the f_t behavior of the device is designed to be flat), there is a tradeoff in optimizing second- and third-order distortions. A more detailed analysis of high-frequency distortion in HBTs will be presented in [9].

IV. Design Strategy for Linear Broad-Band Amplifier

The design methodology for a linear broad-band power amplifier takes advantage of the peaks in the second- and third-order distortion presented in Section III. Two 24-dBm four-stage distributed power amplifiers optimized for second- and third-order distortions were designed with a decade of bandwidth. To minimize the distortion from $C_{\rm BC}$, $V_{\rm CE}$ is set high to fully deplete the collector. This condition is easily met in this design since $V_{\rm CE}$ has to be set as high as possible to maximize output power. Considering the breakdown voltage of the device, a $V_{\rm CE}$ value of 7.5 V was chosen for the design. The bias current is selected by considering the maximum power and load line for class-A operation. Since the power requirements are limited by the load (50 Ω) and bias voltage, both amplifiers are designed to have the same bias current conditions. Determining the current *density* bias then becomes the critical design point to achieve high linearity. As mentioned in Sections II and III, to minimize the second harmonic distortion, the current density should be set where the f_t peaks (at Bias A) and to minimize third harmonic and third-order intermodulation (IM3) distortions, current density should be set at Bias B. Setting the current density is done by properly scaling the areas of each cell.

After the bias points are selected, the input and output matchings are done using standard distributed amplifier design methodology. A major design issue for HBT distributed amplifiers is that the diffusion capacitance dominates the effective input capacitance [10]. This limits the bandwidth of the amplifier. The limitation is further exacerbated for power amplifiers since the diffusion capacitance is proportional to the bias current. To alleviate this problem, a coupling capacitor is placed in series with the input to reduce the effective input capacitance at the cost of gain [11]. Emitter resistor ballasting further reduces diffusion capacitance, though its main purpose is for thermal management. To simplify testing, the biasing of the input and output is achieved through bias tees.

In the design process, it is beneficial to use an HBT model that accounts for effects that influences the shape of the f_t versus

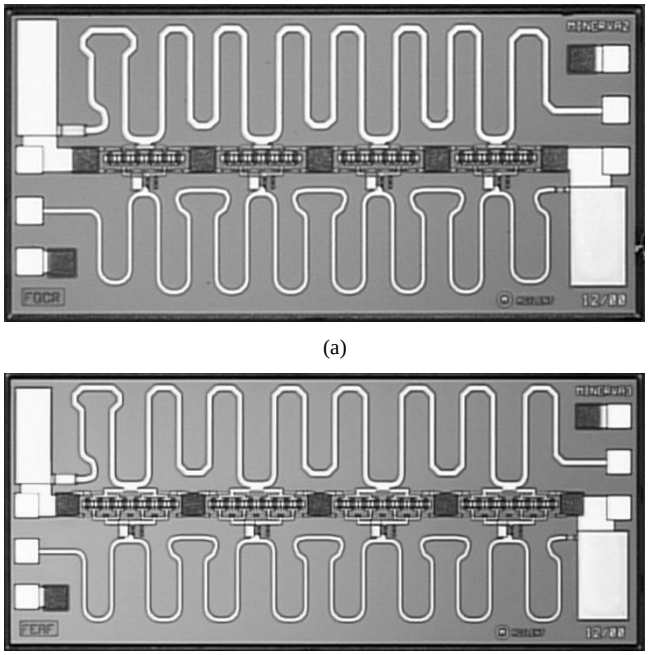

(a)

(b)

Fig. 8. (a) Photograph of second-order amplifier MMIC. (b) Photograph of third-order amplifier MMIC.

I_C curve, such as field-dependent electron velocity and the Kirk effect. An HBT model that includes these effects [12] was used in the design process to accurately identify the appropriate bias currents for optimum linearity.

Photographs of the completed monolithic microwave integrated circuits (MMICs) are shown in Fig. 8(a) and (b) for the second- and third-order amplifiers, respectively. The area of each cell of the second-order amplifier is $6 \times 2 \times 14$ μm^2 and $8 \times 2 \times 16$ μm^2 for the third-order amplifier. The chip sizes of the MMICs are 1.92×0.96 mm^2 and 2.14×0.95 mm^2 for the second- and third-order amplifiers, respectively.

V. Experimental Results

Measurement results for the amplifier that minimizes second-order nonlinearity (DA2H) and for the amplifier that minimizes third-order nonlinearity (DA3H) are summarized in Sections V-A and B.

A. Second-Order Amplifier

The frequency response of the amplifier was evaluated using an Agilent 8510C network analyzer. Although DA2H was optimally designed for low second harmonic distortion (Bias A), it can also be biased at the optimal third-order distortion point (Bias B) by reducing the current to the appropriate value. Fig. 9 shows the S-parameters measured at the two bias points. It is evident that the S-parameters for the two biases look very similar although the bias current densities are different. This is attributed to the fact that the input and output impedances of each stage are predominantly determined by the value of the coupling capacitor and the emitter ballasting resistors. The gain is

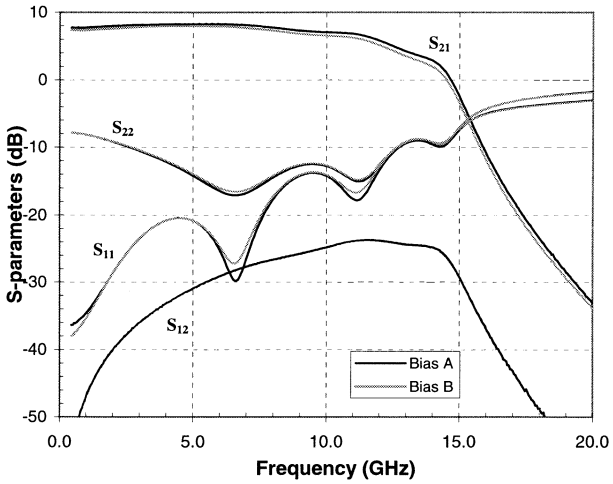

Fig. 9. Measured s-parameters of DA2H at Bias A and Bias B.

7.5±1 dB with 0.5–11-GHz bandwidth. Good input and output matches are also obtained within this bandwidth.

Harmonic-distortion measurements were made at the two bias points. Fig. 10(a) shows a single-tone power sweep at 1 GHz and Fig. 10(b) shows a similar measurement at 5 GHz. At 1 GHz, $P_{1\,\mathrm{dB}}$ is at 25 dBm for Bias A and 23 dBm for Bias B. Although the two bias points have similar gain, it is evident that the second and third harmonic-distortion components are strikingly different. For Bias A, the second harmonic-distortion component is low, while the third harmonic-distortion power is relatively high. Since each cell is biased at the f_t peak, this behavior is consistent with the characteristics observed in Fig. 7. For Bias B, the converse of what is observed for harmonic distortion in Bias A occurs. Relative to Bias A, the second harmonic distortion worsens due to an increase in the slope of f_t versus J_C, and the third harmonic distortion improves due to a decrease in the curvature of f_t versus J_C. It can be observed that the improvement or degradation in distortion power is very significant (10–20 dB) between the two bias points. Also, this biasing technique is effective in controlling harmonic distortion for a wide range of output power. At higher output power, it is evident that the second harmonic deviates from a 2 : 1 slope and the third harmonic deviates from a 3 : 1 due to large-signal nonlinearities caused by higher order distortion terms. Similar trends in biasing are observed at 5 GHz, as seen in Fig. 10(b). At this frequency, $P_{1\,\mathrm{dB}}$ of the amplifier is 24.5 dBm for Bias A and 22.5 dBm for Bias B. At $P_{1\,\mathrm{dB}}$ of Bias A at 5 GHz, a power-added efficiency (PAE) of 14.1% was measured. This relatively low PAE is attributed to the inherent inefficiencies of the standard distributed amplifier topology and the class-A bias point. Much higher values of PAE can be obtained by biasing at a lower quiescent current and designing more optimum input and output matching networks.

To further understand the effectiveness of this broad-band design approach, harmonic and intermodulation distortions were measured at small power levels over frequency. Fig. 11(a) shows the second harmonic intercept (IP2h), third harmonic intercept (IP3h), and third order (intermodulation) intercept point (IP3). The tradeoffs in optimizing the second- and third-order distortions are again evident between the two bias points. It can be

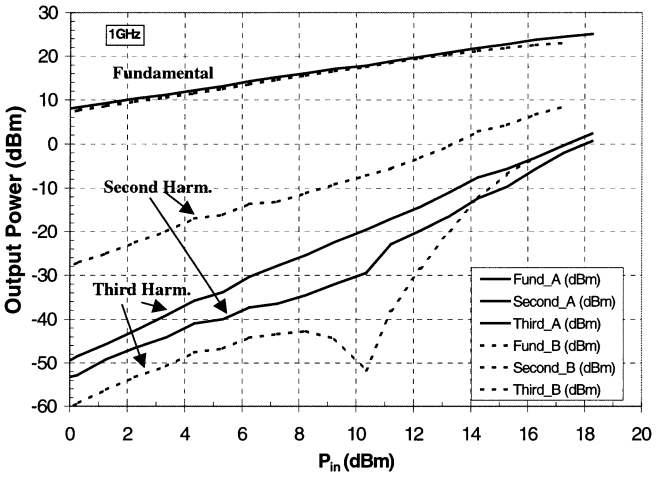

(a)

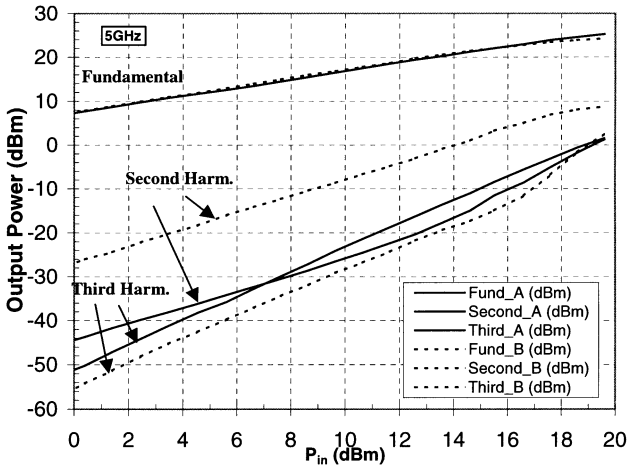

(b)

Fig. 10. (a) Measured fundamental, second harmonic, and third harmonic power versus input power at 1 GHz for Bias A and Bias B. (b) Measured fundamental, second harmonic, and third harmonic power versus input power at 5 GHz for Bias A and Bias B.

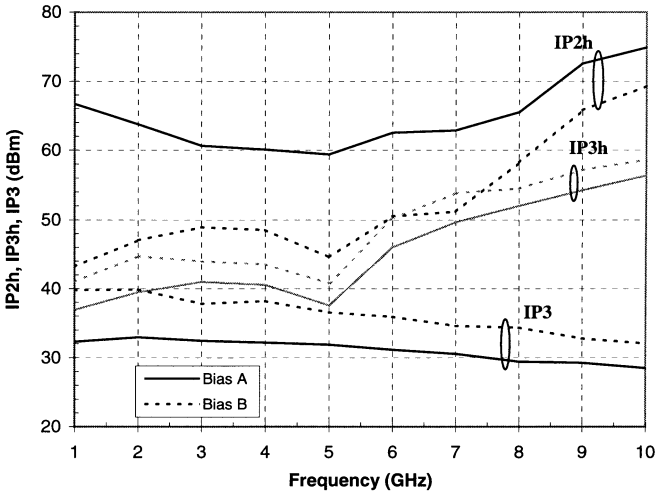

(a)

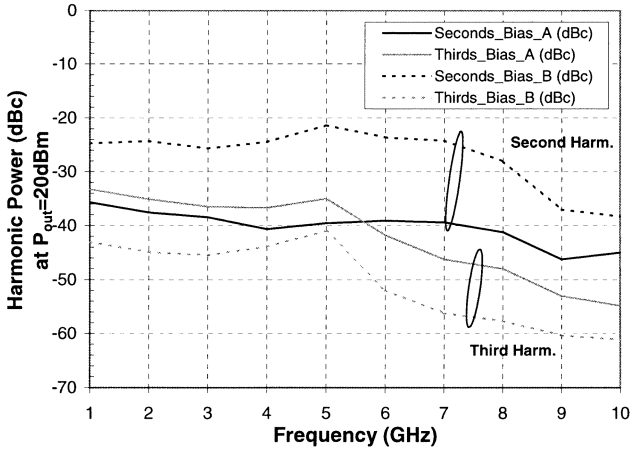

(b)

Fig. 11. (a) Measured IP2h, IP3h, and IP3 versus frequency at Bias A and Bias B. (b) Measured second and third harmonic distortion versus frequency at a fundamental power of 20 dBm at Bias A and Bias B.

seen that this tradeoff is consistent over a wide range of frequencies. Fig. 11(b) shows second and third harmonic distortions measured at a fixed fundamental power of 20 dBm over frequency. This fundamental output power level is large-signal since it is only several decibels backed off from $P_{1\ \mathrm{dB}}$. Similar trends are observed between the two bias points and over frequency.

B. Third-Order Amplifier

Fig. 12 shows an S-parameter measurement of DA3H taken at Bias B, which is the optimum linearity bias point for this amplifier. The gain between 0.5–11-GHz bandwidth is 5.3$\pm$0.5 dB. The reduced gain compared to DA2H is attributed to the fact that the area of each cell of DA3H is significantly larger. However, the general shape of the S-parameters look similar since they are based on the same design.

Fig. 13 shows second and third harmonics versus output power at 5 GHz for DA2H and DA3H at Bias A and Bias B, respectively. The harmonics are plotted against output power since the two amplifiers have dissimilar gains. $P_{1\ \mathrm{dB}}$ for DA3H is 25 dBm at 5 GHz, which is close to the one obtained for

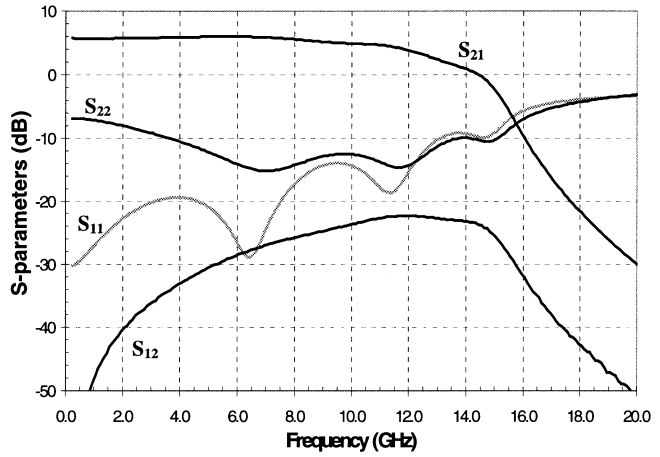

Fig. 12. Measured s-parameters of DA3H at Bias B.

DA2H at Bias A. More importantly, it is evident that the biasing scheme is effective in optimizing the harmonic distortion levels, where low third harmonic distortion is achieved at a cost of second harmonic distortion. At a given output power, the relative difference between DA2H and DA3H in harmonic

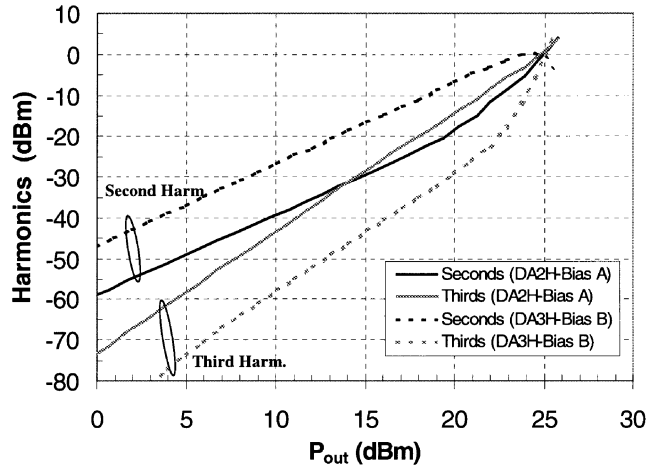

Fig. 13. Comparison of measured second and third harmonic distortions of DA2H at Bias A and DA3H at Bias B at 5 GHz.

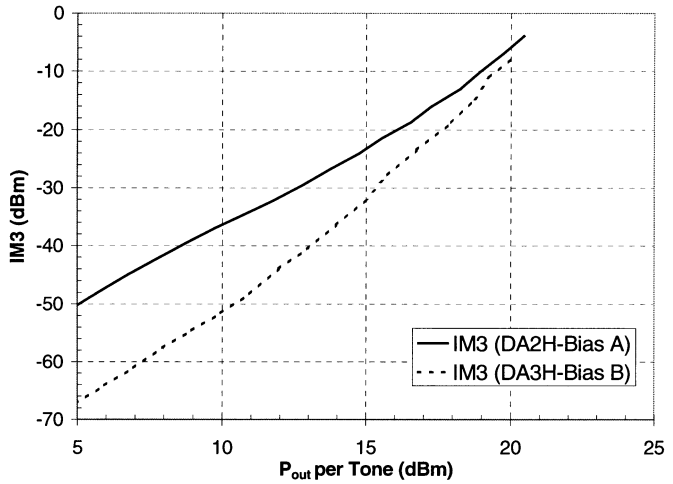

Fig. 14. Comparison of measured IM3 distortion of DA2H at Bias A and DA3H at Bias B at 5 GHz with 1-MHz tone spacing.

power is greater than 10 dB over a wide power range. Fig. 14 shows IM3 distortion measurements of the two amplifiers at 5 GHz with 1-MHz tone spacing. As expected from the results of discrete devices, DA3H at Bias B has significantly better IM3 over a wide power range than DA2H at Bias A. The experimental results from this design technique indicate that DA3H achieves very good IM3 performance at the cost of increased second harmonic distortion.

VI. Conclusions

A design approach for a linear InGaP/GaAs HBT broad-band power amplifier has been presented. The circuit is based on the distributed amplifier topology, and optimum linearity is achieved through careful observation of the nonlinear bias dependence of the base–collector charge. With this biasing method, there is an inherent tradeoff in optimizing the second- and third-order distortion components. Measurements indicate that this biasing technique is applicable over a wide range of frequencies. Ultimately, to minimize the high-frequency distortion in HBTs, the bias dependence of $C_{\rm BC}$ and f_t should be minimized.

Acknowledgment

The authors appreciate the valuable assistance of J. Orr, C. Bourde, and D. Scherrer (for advice on circuit design), D. Davis and V. Moir (for layout issues), J. Wood and X. Qin (for passive model definitions), and A. Cognata (for measurements), all of Agilent Technologies, Santa Rosa, CA. They also greatly appreciate the support and encouragement of D. Root, B. Hughes, Santa Rosa, CA, T. Shirley, D. Hornbuckle, and J. Gladstone, all of Agilent Technologies, and L. Larson, University of California at San Diego, La Jolla.

References

[1] N. L. Wang, W. J. Ho, and J. A. Higgins, "AlGaAs/GaAs HBT linearity characteristics," *IEEE Trans. Microwave Theory Tech.*, vol. 42, pp. 1845–1850, Oct. 1994.

[2] J. Lee, W. Kim, Y. Kim, T. Rho, and B. Kim, "Intermodulation mechanism and linearization of AlGaAs/GaAs HBT's," *IEEE Trans. Microwave Theory Tech.*, vol. 45, pp. 2065–2072, Dec. 1997.

[3] W. Kim, S. Kang, K. Lee, M. Chung, Y. Yang, and B. Kim, "The effects of $C_{\rm BC}$ on the linearity of AlGaAs/GaAs power HBT's," *IEEE Trans. Microwave Theory Tech.*, vol. 49, pp. 1270–1276, July 2001.

[4] M. Iwamoto, T. S. Low, C. P. Hutchinson, J. B. Scott, A. Cognata, X. Qin, L. H. Camnitz, P. M. Asbeck, and D. C. D'Avanzo, "Linearity characteristics of InGaP/GaAs HBT's and the influence of collector design," *IEEE Trans. Microwave Theory Tech.*, vol. 45, pp. 2377–2388, Dec. 2000.

[5] C. T. Kirk, Jr, "A theory of transistor cutoff frequency (F_T) falloff at high current densities," *IRE Trans. Electron Devices*, vol. ED-9, pp. 164–174, 1962.

[6] M. Schröter, D. Pehlke, and T.-Y. Lee, "Compact modeling of high-frequency distortion in silicon integrated bipolar transistors," *IEEE Trans. Electron Devices*, vol. 47, pp. 1529–1535, July 2000.

[7] R. Katoh, "Charge-control analysis of collector transit time for (AlGa)As/GaAs HBT's under a high injection current," *IEEE Trans. Electron Devices*, vol. 37, pp. 2176–2182, Oct. 1990.

[8] L. H. Camnitz and N. Moll, "An analysis of the cutoff-frequency behavior of microwave heterostructure bipolar transistors," in *Compound Semiconductor Transistors, Physics and Technology*. Piscataway, NJ: IEEE Press, 1993, pp. 21–46.

[9] M. Vaidyanathan, M. Iwamoto, L. E. Larson, P. S. Gudam, and P. M. Asbeck, "High-frequency distortion in bipolar transistors," *IEEE Trans. Microwave Theory Tech.*, submitted for publication.

[10] J. P. Viaud, M. Lajugie, R. Quéré, and J. Obregon, "First demonstration of a 0.5 W, 2 to 8 GHz MMIC HBT distributed power amplifier based on a large signal design approach," in *IEEE MTT-S Int. Microwave Symp. Dig.*, June 1997, pp. 893–896.

[11] Y. Ayasli, S. W. Miller, R. Mozzi, and L. K. Hanes, "Capacitively coupled traveling-wave power amplifier," *IEEE Trans. Electron Devices*, vol. ED-31, pp. 1937–1942, Dec. 1984.

[12] L. H. Camnitz, S. Kofol, T. S. Low, and S. R. Bahl, "An accurate, large signal, high frequency model for GaAs HBT's," in *GaAs IC Symp. Tech. Dig.*, 1996, pp. 303–306.

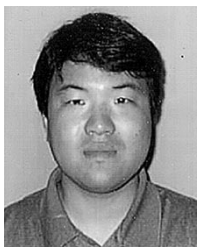

Masaya Iwamoto (S'99) received the B.S. degree in electrical engineering from Cornell University, Ithaca, NY, in 1997, the M.S. degree in electrical engineering from the University of California at San Diego (UCSD), La Jolla, in 1999, and is currently working toward the Ph.D. degree at UCSD. His doctoral dissertation concerns the distortion characteristics of InGaP/GaAs HBTs and their applications to power amplifiers.

During the summers of 1997–2002, he was an Intern with Agilent Technologies (formerly Hewlett-Packard), Santa Rosa, CA, where his responsibilities included HBT large-signal modeling, distortion characterization, and broad-band power-amplifier design.

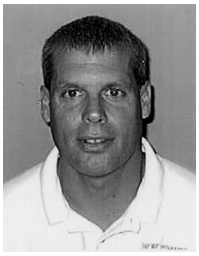

Craig P. Hutchinson received the B.S. degree in electrical engineering form the University of California, Davis (UCD), in 1984.

In 1984, he joined Avantek, where he designed broad-band GaAs integrated circuits, including amplifiers, switches, and attenuators. In 1988, he joined Pacific Monolithics, where he was responsible for the design of GaAs integrated circuits, including mixers, amplifiers, oscillators, and transmit/receive (T/R) modules. Since the fall of 1990, he has been with Avantek/Hewlett-Packard/Agilent Technologies, Santa Rosa, CA, where he designs high-speed silicon bipolar GaAs MESFETs. Since 1996, he has been involved with the design of GaAs HBT integrated circuits for Agilent's instrumentation product lines.

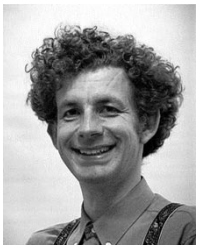

Jonathan B. Scott (S'90–M'97–SM'98) was born in Brisbane, Australia, in 1956. He received the B.Sc., B.E., Master of Engineering, and Ph.D. degrees from the University of Sydney, Sydney, N.S.W., Australia, in 1977, 1979, 1986, and 1997, respectively.

He was with the Air Navigation Group, a research arm of the Department of Transport, where he was involved with microwave transient digitization. He was a consultant in a variety of industries, including radar and analog signal processing. He then became Manager of the Sydney Microwave Design Resource Centre from 1988 to 1992, as well as a Senior Lecturer with the Department of Electrical Engineering, University of Sydney. He was involved in establishing and subsequently teaching in the Graduate Program in Audio, School of Architectural and Design Science. In 1995, he was a visitor with University College London, London, U.K. He subsequently became a Visiting Lecturer with the University of Western Sydney. In 1994, he was with Macquarie University, where he was involved with nonlinear electronic systems and assisted in the setup of the Collaborative Nonlinear Electronic Research Facility (CNERF) in conjunction with the Electronics Department, Macquarie University, and Macquarie Research Limited. In 1997, became Chief Engineer with RF Technology Ltd. In 1999, he joined the Microwave Technology Division, Hewlett-Packard (now Agilent Technologies), Santa Rosa, CA. He has authored over 50 refereed publications and an undergraduate textbook.

Dr. Scott is a Fellow of the Institution of Engineers, Australia. He is a member of the Audio Engineering Society (AES). He is an Honorary Associate of Macquarie University. He has served on committees of the Standards Association of Australia. He was the recipient of a 1993 British Telecom Research Fellowship and the 1994 Electrical Engineering Foundation Medal for Excellence in Teaching.

Thomas S. Low was born in Rockford, IL, in 1951. He received the B.S. degree in physics from Purdue University, West Lafayette, IN, in 1975, the M.S. and Ph.D. degrees in physics from the University of Illinois at Urbana-Champaign, in 1978 and 1984, respectively.

He was with Hewlett-Packard Laboratories, Palo Alto, CA, until 1989, during which time he provided semiconductor characterization support to several epi-growth developments, including MOCVD and molecular beam epitaxy (MBE) pseudomorphic high electron-mobility transistors (pHEMTs), Be-doped AlGaAs HBTs, and InGaAs p-i-n photodetectors. In 1989, he joined Hewlett-Packard's Microwave Technology Center, Santa Rosa, CA, to aid with the transfer of HBT integrated circuit (IC) process and epi-growth technology to the manufacturing site, which culminated in an InGaP HBT IC production release in 1998. He is currently with Agilent Technologies, Santa Rosa, CA. His current interests include process design and device physical modeling of InGaP HBT ICs and various other optical and electronic heterojunction devices.

Mani Vaidyanathan (S'95–M'99) is currently an Assistant Research Scientist with the University of California at San Diego, La Jolla. His research interests are the theory and modeling of semiconductor devices, where he has been involved with topics ranging from describing carrier transport in small-dimension transistors to characterizing nonlinear behavior for RF applications.

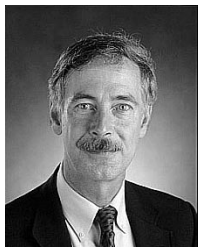

Peter M. Asbeck (M'75–SM'97–F'00) received the B.S. and Ph.D. degrees from the Massachusetts Institute of Technology (MIT), Cambridge, in 1969 and in 1975, respectively.

His professional experience includes working with the Sarnoff Research Center, Princeton, NJ, and Philips Laboratory, Briarcliff Manor, NY. In 1978, he joined the Rockwell International Science Center, Thousand Oaks, CA, where he was involved in the development of high-speed devices and circuits using III–V compounds and heterojunctions. He pioneered the effort to develop HBTs based on GaAlAs/GaAs and InAlAs/InGaAs materials. In 1991, he joined the University of California at San Diego, La Jolla, as a Professor in the Department of Electrical and Computer Engineering. His research has led to over 220 publications.

Dr. Asbeck is a Distinguished Lecturer of the IEEE Electron Devices Society and the IEEE Microwave Theory and Techniques Society (IEEE MTT-S).

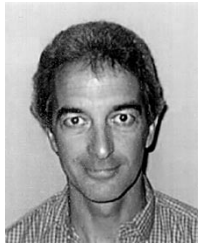

Donald C. D'Avanzo (S'72–M'78) received the B.S. degree in biomedical engineering from Brown University, Providence, RI, in 1973, and the M.S. and Ph.D. degrees in electrical engineering from Stanford University, Stanford, CA, in 1974 and 1980, respectively. His doctoral research included characterization and modeling of V-groove metal–oxide semiconductor (VMOS) and double-diffused metal–oxide semiconductor (DMOS) transistors and spreading resistance measurements development and data analysis.

Since March 1979, he has been with the Microwave Technology Center, Agilent Technologies (formerly Hewlett-Packard), Santa Rosa, CA, initially as a Member of the Technical Staff. Since 1982, he has served as the Research and Development Project Manager responsible for the development of new GaAs IC technologies including MESFETs, pHEMTs, HBTs, and diodes. He has authored or coauthored numerous publications and presentations. He holds patents in the field of GaAs IC technology.

Dr. D'Avanzo is a member of Tau Beta Pi, Sigma Xi, and the Electrochemical Society. He has served on the Technical Program Committees of the GaAs IC Symposium, the IEEE Microwave Theory and Techniques Society (IEEE MTT-S) International Microwave Symposium (IMS) and the Topical Workshop on Heterojunction Microelectronics. He has served as the symposium chairman of the IEEE GaAs IC Symposium and the Electrochemical Society State of the Art Symposium on Compound Semiconductors.